ADVANCING EARTH AND SPACE SCIENCES

JGR Oceans

RESEARCH ARTICLE
10.1029/2026JC024014

The Effect of the Earth's Rotation on Wave-Induced Drift in Finite-Depth Water: The Role of Unsteadiness

J. Mol[1], J. J. M. Slot[2], P. A. Sanders[3], M. Duran-Matute[3], and T. S. van den Bremer[1]

[1]Faculty of Civil Engineering and Geosciences, Delft University of Technology, Delft, The Netherlands, [2]Department of Mathematics and Computer Science, Eindhoven University of Technology, MB Eindhoven, The Netherlands, [3]Department of Applied Physics and Science Education, Eindhoven University of Technology, MB Eindhoven, The Netherlands

Key Points:

- We derive a model for the time-dependent drift velocity induced by a time-varying surface wave forcing on a rotating Earth
- The wave-induced drift velocity contains damped inertial oscillations, which decay faster in finite-depth water
- Including the effect of finite depth can have a significant impact on the predicted surface transport near the coast

Supporting Information:

Supporting Information may be found in the online version of this article.

Correspondence to:

J. Mol,
j.mol@tudelft.nl

Citation:

Mol, J., Slot, J. J. M., Sanders, P. A., Duran-Matute, M., & van den Bremer, T. S. (2026). The effect of the Earth's rotation on wave-induced drift in finite-depth water: The role of unsteadiness. *Journal of Geophysical Research: Oceans*, *131*, e2026JC024014. https://doi.org/10.1029/2026JC024014

Received 12 JAN 2026
Accepted 19 JUN 2026

Author Contributions:

Conceptualization: J. Mol, J. J. M. Slot, M. Duran-Matute, T. S. van den Bremer
Formal analysis: J. Mol, J. J. M. Slot, P. A. Sanders
Funding acquisition: T. S. van den Bremer
Investigation: J. Mol, J. J. M. Slot, P. A. Sanders
Methodology: J. Mol
Supervision: J. J. M. Slot, M. Duran-Matute, T. S. van den Bremer
Writing – original draft: J. Mol
Writing – review & editing: J. Mol, J. J. M. Slot, P. A. Sanders, M. Duran-Matute, T. S. van den Bremer

Abstract Wave-induced transport in the coastal zone can play an important role in the distribution of nutrients, plankton, and pollutants including plastic litter. The effect of the water depth, unsteadiness of the wave field, and the rotation of the Earth on the wave-induced drift is investigated in this paper. We derive a model for the time-dependent drift velocity in finite-depth water for a time-varying wave forcing, where we include the effect of rotation and a constant eddy viscosity. The solution is given in the form of a finite-depth Ekman-Stokes kernel. Convolution of this kernel with a time series of the Stokes drift gives the wave-induced Eulerian-mean velocity. The resulting unsteady flow contains damped inertial oscillations, where the amplitude of the oscillations is influenced by the rate of change of the wave forcing. Both a decrease in water depth (lower kh) and a decrease in the relative importance of rotation compared to viscosity (lower (inverse) wave Ekman number Ek^{-1}) lead to faster decay of these oscillations. Applying the model to buoy data shows a large impact on the predicted transport in finite depth.

Plain Language Summary To understand the distribution of particles in the ocean such as nutrients, plankton, and pollutants including plastic litter, we need to know how they are transported. The coastal zone can play a role in this distribution, since it connects the shore to the deep ocean. One of the important processes in this region is the transport by waves. We derive a mathematical model for wave-induced transport near the coast, where we take the rotation of the Earth and the time variation of the both the drift and the wave field into account. Particles near the water surface are transported to the right of the wave direction (on the Northern Hemisphere), while describing damped inertial oscillations. Both a smaller water depth and a lower relative importance of rotation compared to viscosity can make these oscillations disappear faster. However, it is the combination of both of these effects that ultimately determines how quickly these oscillations decay. Applying the model to buoy data shows a large impact on the predicted transport when considering coastal regions.

1. Introduction

Accurate prediction of the distribution of pollutants such as plastic (van Sebille et al., 2020), nutrients (Gruber et al., 2011) and plankton (Nooteboom et al., 2019) requires an understanding of physical processes leading to particle transport in the ocean. The coastal zone links the shore to the open ocean and can act as an important source and/or sink of pollutant particles. The coastal zone can therefore play a potentially very large role in the distribution of these particles across the oceans. For example, large floating marine plastic has been found to be more abundant in coastal waters, suggesting that the nearshore region could act as a sink for such plastics (Morales-Caselles et al., 2021).

There are many different processes that drive transport in the coastal zone, spanning a wide range of scales, from large-scale currents to small-scale turbulence (DiBenedetto, 2025; Moulton et al., 2023). One of the important processes is the transport due to surface gravity waves. The unclosed orbital motion of a particle underneath a wave gives rise to a net drift in the wave direction known as Stokes drift (Stokes, 1847; van den Bremer & Breivik, 2017). The combination of the Stokes drift with a background rotation, such as the rotation of the Earth, causes an additional wave-induced Eulerian-mean velocity (Hasselmann, 1970; Higgins et al., 2020; Lewis & Belcher, 2004; Ursell, 1950; Xu & Bowen, 1994). Together, they determine the wave-induced transport of a particle by the Lagrangian-mean velocity

$$\overline{\boldsymbol{u}}_L = \boldsymbol{u}_S + \overline{\boldsymbol{u}}_E, \quad (1)$$

where $\overline{\{\}}$ denotes a wave average, $\boldsymbol{u}_S$ is the Stokes drift and $\overline{\boldsymbol{u}}_E$ the wave-induced Eulerian-mean velocity. The wave-induced transport is not only influenced by the rotation of the Earth, but also by viscosity and the water depth. We will discuss the effect of including these physical processes in the following paragraphs.

The impact of the Earth's rotation on wave-induced transport was first considered by Ursell (1950), who argued that conservation of circulation leads to the requirement that there can be no steady Lagrangian-mean velocity in an inviscid rotating ocean. Hasselmann (1970) showed that, under rotation, the wave-averaged Reynolds stress is not zero, leading to the Coriolis–Stokes force. The resulting inviscid wave-averaged Lagrangian flow describes an inertial oscillation. Averaging over this inertial circle leads to a zero Lagrangian-mean velocity, in agreement with Ursell (1950), due to the cancellation of the Stokes drift by the (inertially averaged) Eulerian-mean velocity at every depth. This Eulerian-mean velocity is sometimes referred to as the "anti-Stokes drift." The effect of viscosity on wave-induced drift was studied by Longuet-Higgins (1953) for water of finite depth in a non-rotating frame. He showed that the viscous bottom boundary layer leads to a (Eulerian-mean) streaming velocity close to the bottom, and the viscous surface boundary layer leads to a wave stress just below the surface, which both effect the Lagrangian-mean velocity (see also Phillips, 1977).

Combining the effects of both rotation and viscosity on the wave-induced transport in deep water shows that a non-zero viscosity causes a non-zero net mass transport, in contrast to the inviscid solution (Jenkins, 1986; Madsen, 1978; Weber, 1983a, 1983b, 2019). Extending previous work by allowing for any given time variation of the wave forcing, Higgins et al. (2020) derived a kernel solution for the time-dependent Eulerian-mean velocity in deep water. Using observational data to estimate the Stokes drift, Cunningham et al. (2022) applied this Ekman–Stokes kernel and showed that the inclusion of the wave-induced Eulerian-mean flow in particle tracking simulations has a significant impact on the distribution of floating plastic in the ocean. Alternatively, a fully coupled ocean-wave model can be used to include the wave-induced Eulerian-mean flow in simulations (e.g., Breivik et al., 2015; Drivdal et al., 2014; Rühs et al., 2025). Rühs et al. (2025) show that the Stokes drift and wave-induced Eulerian current have a significant impact on the surface particle dispersal. They emphasize the need to include both effects, since including only the Stokes drift might not improve the dispersal predictions compared to not including any wave effect at all.

In realistic ocean conditions, the turbulence in the mixed surface layer should also be considered. The effect of turbulence can be captured by an eddy viscosity, which combines the molecular viscosity with the effect of turbulence. For simplicity, the eddy viscosity is often assumed to be constant. However, the local level of turbulence is better represented by a depth-dependent eddy viscosity (Craig & Banner, 1994). For that reason, Lewis and Belcher (2004) and Polton et al. (2005) extend previous work by providing a steady solution for a linearly varying eddy viscosity. By comparing their solutions to observational data, they also demonstrate the importance of the inclusion of the Coriolis–Stokes force. On the inner continental shelf, the importance of including the Coriolis–Stokes force has also been demonstrated in the analysis of field observations by Lentz et al. (2008). They measured a Eulerian-mean flow with the same vertical structure as the Stokes drift, but in the opposite direction (anti-Stokes) and showed that this is consistent with a steady balance between Coriolis and Coriolis–Stokes forces.

The recent studies by Higgins et al. (2020), Cunningham et al. (2022) and Rühs et al. (2025) highlight the importance of including the effect of rotation when considering the time-dependent wave-induced transport, but focus on deep-water conditions. In coastal regions, the effect of finite depth also plays an important role. Xu and Bowen (1994) provide a steady solution for the Eulerian-mean velocity in finite-depth water, by combining the rotating, inviscid solutions of Ursell (1950) and Hasselmann (1970) with the non-rotating viscous solutions of Longuet-Higgins (1953). However, this analysis has not been explicitly extended to include time dependence of the wave forcing and the Eulerian-mean velocity that results from this, as has been done by Weber (1983a) and Higgins et al. (2020) for deep water. Xu and Bowen (1994) do consider the unsteady effects arising for a suddenly imposed steady wave forcing (formulated as an eigenvalue problem) and note that their solution can, in principle, be extended to any time-varying forcing through superposition. Their solution is given in the form of an integral that is left unevaluated. Beyond identifying its main features, Xu and Bowen (1994) do not investigate the effects of unsteadiness, finite depth, their interaction, and its implications for wave-induced transport, which are the focus of the present paper.

In this paper, we derive a model for the time dependent wave-induced transport in finite-depth water for any given time variation of the Stokes drift forcing, following the same approach as Higgins et al. (2020). Hence, it forms a link between the finite-depth solution by Xu and Bowen (1994) and the time-dependent solution by Higgins et al. (2020). We show that our solution recovers the solution of Xu and Bowen (1994) if the integral that makes up their solution is explicitly evaluated (Appendix A). We provide the solution in the form of what we call the finite-depth Ekman–Stokes kernel (Section 3.1). This kernel can be applied in the same way as the Higgins et al. (2020) deep-water kernel, as was done by Cunningham et al. (2022), but now for regions with a smaller water depth, such as near coasts. Additionally, we derive and analyze the solutions for the Eulerian-mean velocity for both a suddenly imposed constant wave forcing (Section 4.1) and a suddenly imposed viscously attenuated wave forcing (Section 4.2). We present a detailed analysis of the unsteady flow in finite depth through the application of the finite-depth kernel to an idealized storm (Section 5.1) and to a Stokes drift time series estimated from buoy data (Section 5.2).

2. Governing Equations

We consider waves on a sea with a constant, finite water depth h, in a Cartesian coordinate system, where x and y are the horizontal coordinates, and the vertical coordinate z is directed upwards from the undisturbed water surface. In the Eulerian framework, the governing equations for an incompressible, viscous, rotating fluid of constant density ρ are the Navier–Stokes and continuity equations, given by.

$$\frac{\partial \mathbf{u}}{\partial t} + \mathbf{u}\cdot\nabla\mathbf{u} + \mathbf{f}\times\mathbf{u} = -\frac{1}{\rho}\nabla(p+\rho g z) + \nu\nabla^2\mathbf{u}, \tag{2}$$

$$\nabla\cdot\mathbf{u} = 0, \tag{3}$$

where $\mathbf{u} = (u, v, w)$ is the three-dimensional velocity vector, $\mathbf{f} = (0, 0, f)$ is the Coriolis vector with f the Coriolis parameter, p is the pressure, g is the acceleration due to gravity and ν is the eddy viscosity, which we assume to be constant. From these equations, Xu and Bowen (1994) derive the equations for the drift velocity in finite-depth water subject to a background rotation. Taking the wave average of Equations 2 and 3 and assuming that the horizontal variations are much smaller than the vertical variations gives the mean flow equations. Using the solution to the linearized equations for the wave orbital velocities to rewrite the Reynolds stresses leads to the Stokes–Coriolis force in the interior (Hasselmann, 1970) and the streaming velocity above the bottom boundary (Longuet-Higgins, 1953; Phillips, 1977). Assuming a free surface without explicit external forcing of the waves leads to the (virtual tangential) wave stress just below the surface (Longuet-Higgins, 1953; Xu & Bowen, 1994). Retaining not only rotation and the effect of the eddy viscosity, but also time variation, the wave-averaged equations for the Eulerian-mean velocity outside the boundary layers are then given by (Hasselmann, 1970; Higgins et al., 2020; Longuet-Higgins, 1953; Weber et al., 2015; Xu & Bowen, 1994)

$$\left(\partial_t + if - \nu\partial_z^2\right)\overline{U}_E(z,t) = -ifU_S(z,t), \tag{4}$$

$$\partial_z\overline{U}_E(z,t) = \partial_z U_S(z,t) \qquad \text{at } z = \eta - \delta_\nu \ \approx\ 0, \tag{5}$$

$$\overline{U}_E(z,t) = \frac{3}{2}U_S(z,t) \qquad \text{at } z = -h + \delta_\nu \ \approx -h, \tag{6}$$

where η is the free surface elevation, $\delta_\nu = \sqrt{2\nu/\omega}$ is the thickness of the (wave-driven) boundary layer, and we use the complex notation $U_E = \overline{u}_E + i\ \overline{v}_E$ for the horizontal wave-induced Eulerian-mean velocity and $U_S = u_S + i\ v_S$ for the Stokes drift. Equations 4–6 are identical to those derived by Xu and Bowen (1994, Equations 68–70) for wave-driven flow (zero wind stress), aside from the inclusion of the time derivative and exclusion of the region inside the bottom boundary layer. The boundary conditions (Equations 5 and 6) of Longuet-Higgins (1953) are applied at the edge of the thin boundary layers. As a consequence, the solution to the Ekman–Stokes equation (Equation 4) is only valid outside the boundary layers. It is possible to solve for the velocity inside both the surface and the bottom boundary layer (Weber, 1983a, 1983b, 2019; Xu & Bowen, 1994). However, since a Lagrangian framework would be more suitable for this, we leave this outside the scope of the present paper.

The wave-averaged "Ekman-Stokes" equation (Equation 4) and the (wave-averaged) surface boundary condition (Equation 5) are identical to those used in Higgins et al. (2020). However, instead of requiring the flow to vanish at large depth as in Higgins et al. (2020), we require the flow to match the bottom streaming velocity at finite depth

$z = -h$. The Eulerian-mean velocity $\overline{U}_E(z,t)$ is, therefore, not only driven by the Coriolis–Stokes force in the interior, but also by the (virtual tangential) wave stress at the surface (Equation 5) and the streaming velocity at the bottom (Equation 6).

3. General Unsteady Solution: The Finite-Depth Ekman–Stokes Kernel

In order to solve Equation 4 subject to the boundary conditions (Equations 5 and 6), we convert the partial differential equation (PDE) to an ordinary differential equation (ODE) using a Laplace transform. The Laplace transform is denoted by a tilde and is defined as

$$\tilde{g}(s) = \mathcal{L}\{g(t)\} = \int_0^\infty g(t)\, e^{-st}\, \mathrm{d}t, \tag{7}$$

for a general function $g(t)$. We consider a suddenly imposed (quasi-) monochromatic wave forcing with an arbitrary time dependence (slow compared to the time scale of the waves) of the wave amplitude and direction, giving a Stokes drift

$$U_S(z,t) = \begin{cases} 0 & t < 0, \\ a^2(t)\omega k \dfrac{\cosh(2k(h+z))}{2\sinh^2(kh)} e^{i\theta(t)} & t \geq 0, \end{cases} \tag{8}$$

with wave amplitude $a(t)$, angular frequency of the wave ω, wavenumber k and wave direction with respect to the x-axis $\theta(t)$. Assuming

$$\overline{U}_E(z, t=0) = 0, \tag{9}$$

and solving the ODE gives a solution in Laplace space of the form

$$\tilde{\overline{U}}_E(z,s) = \tilde{K}(z,s)\, \tilde{U}_S(z=0,s), \tag{10}$$

where we define $\tilde{K}(z,s)$ as the Laplace transform of the Ekman–Stokes kernel for finite-depth water $K(z,t)$. Using the Laplace convolution theorem, we find the Eulerian-mean velocity

$$\overline{U}_E(z,t) = U_S(z=0,t) * K(z,t) = \int_0^t U_S(z=0,T) K(z,t-T)\, \mathrm{d}T, \tag{11}$$

where $*$ denotes a convolution in time.

3.1. Finite-Depth Ekman–Stokes Kernel

To determine the Eulerian-mean velocity for a given Stokes drift, we need to find the expression for the finite-depth Ekman–Stokes kernel given by

$$\begin{aligned} K(z,t) &= \mathcal{L}^{-1}\{\tilde{K}(z,s)\}, \\ &= \frac{1}{2\pi i}\int_{\Upsilon - i\infty}^{\Upsilon + i\infty} \tilde{K}(z,s)\, e^{st}\, \mathrm{d}s, \end{aligned} \tag{12}$$

where we write the inverse Laplace transform as a Bromwich integral along the vertical line in the complex plane such that $\Upsilon \in \mathbb{R}$ is larger than the real part of all singularities of $\tilde{K}(z,s)$. Considering a contour integral that contains the Bromwich line integral and using Cauchy's residue theorem to write this contour integral as the sum of the residues of the enclosed singularities, we find the kernel (see Text S1 in Supporting Information S1).

$$K(z,t) = e^{-ift}\sum_{n=0}^{\infty} e^{-\left(n+\frac{1}{2}\right)^2\pi^2\nu t/h^2}\cos\left(\left(n+\frac{1}{2}\right)\pi\frac{z}{h}\right) \times \nu\left[\frac{4k}{h}\tanh(2kh)+\frac{3}{h^2}\frac{(-1)^n\left(n+\frac{1}{2}\right)\pi}{\cosh(2kh)} - \frac{if/\nu}{\left(n+\frac{1}{2}\right)^2\pi^2+(2kh)^2} \times\left(4kh\tanh(2kh)+2\frac{(-1)^n\left(n+\frac{1}{2}\right)\pi}{\cosh(2kh)}\right)\right] \tag{13}$$

We can non-dimensionalize the kernel using the parameters kh and the (inverse) wave Ekman number, which is a measure of the relative importance of rotation and viscosity and is defined as (Huang, 1979; Mol et al., 2025)

$$Ek^{-1} = \frac{\delta_S^2}{\delta_E^2} = \frac{f}{8\nu k^2}, \tag{14}$$

with the Stokes depth $\delta_S = 1/(2k)$ and the Ekman depth $\delta_E = \sqrt{2\nu/f}$. Rewriting then gives the dimensionless kernel

$$\frac{K(z/h,\tau)}{f} = e^{-i\tau}\sum_{n=0}^{\infty} e^{-\left(n+\frac{1}{2}\right)^2\pi^2\tau/\left(2Ek^{-1}(2kh)^2\right)}\cos\left(\left(n+\frac{1}{2}\right)\pi\frac{z}{h}\right) \times\left[\frac{1}{Ek^{-1}(2kh)^2}\left(2kh\tanh(2kh)+\frac{3}{2}\frac{(-1)^n\left(n+\frac{1}{2}\right)\pi}{\cosh(2kh)}\right) - \frac{2i}{\left(n+\frac{1}{2}\right)^2\pi^2+(2kh)^2}\left(2kh\tanh(2kh)+\frac{(-1)^n\left(n+\frac{1}{2}\right)\pi}{\cosh(2kh)}\right)\right] \tag{15}$$

as a function of z/h, $\tau = ft$. Convolution of the kernel with a given Stokes drift forcing gives the wave-induced Eulerian-mean velocity (Equation 11). Taking the limit $h \to \infty$ of the finite-depth kernel (see Text S4 in Supporting Information S1) recovers the deep-water kernel of Higgins et al. (2020). Xu and Bowen (1994) also give a kernel-like solution for an unsteady wave forcing in their equation 110, but they do not provide a fully computed expression or any further analysis. Explicit computation and rewriting of their expression (not performed therein) can be shown to result in Equation 13 (see Appendix A).

The finite-depth Ekman–Stokes kernel is illustrated in Figure 1. The magnitude and argument of the finite-depth kernel show behavior that is very similar to the deep-water kernel of Higgins et al. (2020), with the magnitude of the kernel decreasing over time and depth and the argument showing an oscillation with the inertial period $2\pi/f$. However, comparing the real and imaginary parts of the finite-depth and deep-water kernels in Figure 1c, we notice that the hodograph of the finite-depth kernel spirals toward the origin much faster. In Section 4.1 and 4.2, we will also see this enhanced damping effect of finite depth in the solutions for a suddenly imposed constant and a suddenly imposed attenuated wave forcing.

4. Solutions for Simplified Forcing Examples

The kernel solution itself does not provide a velocity, since it first needs to be convolved with a time series of the Stokes drift. We will, therefore, consider some simple wave forcing examples that allow us to examine the induced Eulerian-mean velocity. To investigate the time dependence of the drift and the effect of kh and Ek^{-1} without the influence of a time dependence of the forcing (after the initial step function onset), we first consider a (suddenly imposed) constant wave forcing. The second example, with an attenuated wave forcing, illustrates the addition of a (simple) time dependence of the forcing. It also shows the remaining flow after the wave forcing has (almost completely) dissipated.

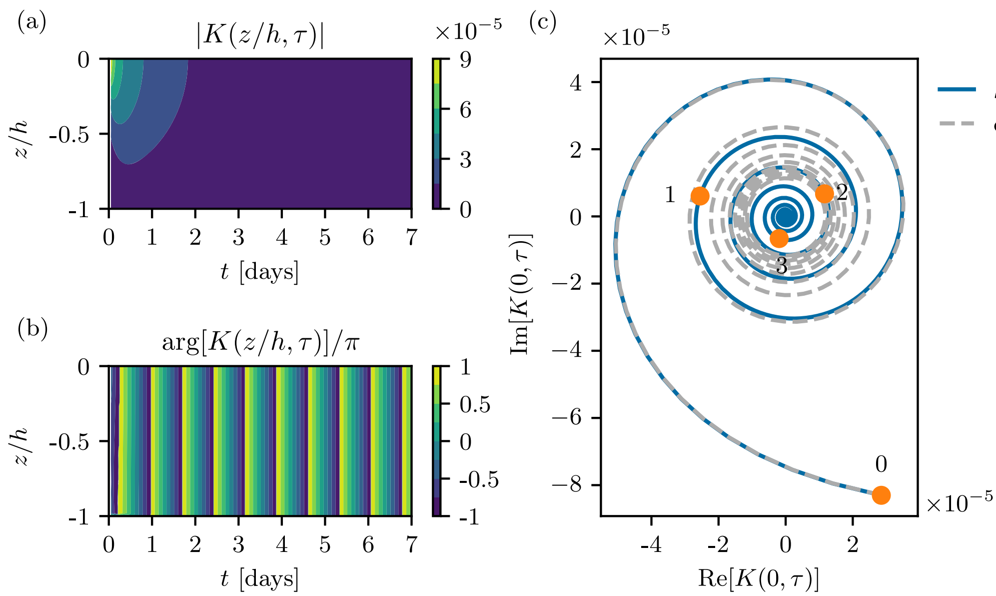

Figure 1. The magnitude (a), argument (b) and hodograph (c) of the finite-depth Ekman-Stokes kernel $K(z/h,\tau)$ for $f = 1 \times 10^{-4}$ rad/s, $Ek^{-1} = 1$ and $kh = 2$. In (c), both the finite-depth kernel and the deep-water kernel of Higgins et al. (2020) are shown (by a blue line and a dashed gray line, respectively) at $z = 0$ for a duration of 7 days. The time (in days) is marked on the hodograph of the finite-depth kernel for the first 3 days (orange dots). It should be noted that $t = 0$ is a singular point.

4.1. Suddenly Imposed Constant Wave Field

The simplest forcing we can consider is a suddenly imposed constant wave field, giving a Stokes drift of

$$U_{S,\mathrm{const}}(z,t) = \begin{cases} 0 & t < 0, \\ U_S(z) & t \geq 0. \end{cases} \tag{16}$$

To find the Eulerian-mean velocity for this specific wave forcing, we calculate the convolution (Equation 11) of the Stokes drift (Equation 16) with the finite-depth kernel. The result consists of an inertial oscillation $(\exp(-i\tau))$ with a time- and z-dependent amplitude and a time independent part $\left(\overline{\overline{U}}_{E,\,\mathrm{steady}}\right)$, which together give the Eulerian-mean velocity (see Texts S2 and S3 in Supporting Information S1)

$$\frac{\overline{U}_{E,\mathrm{const}}(z/h,\tau)}{U_S(z=0)} = e^{-i\tau}\sum_{n=0}^{\infty} e^{-\left(n+\frac{1}{2}\right)^2\pi^2\tau/\left(2Ek^{-1}(2kh)^2\right)}\,\mathcal{F}_{n,\mathrm{const}}\cos\left(\left(n+\frac{1}{2}\right)\pi\frac{z}{h}\right) + \frac{\overline{\overline{U}}_{E,\,\mathrm{steady}}(z/h)}{U_S(z=0)} \tag{17}$$

with

$$\begin{aligned}\mathcal{F}_{n,\mathrm{const}} = &\frac{1}{1+\left(n+\frac{1}{2}\right)^2\pi^2/\left(2iEk^{-1}(2kh)^2\right)} \\ &\times\left[\frac{-2}{2iEk^{-1}(2kh)^2}\left(2kh\tanh(2kh)+\frac{3}{2}\frac{(-1)^n\left(n+\frac{1}{2}\right)\pi}{\cosh(2kh)}\right)\right. \\ &\left.+\frac{2}{\left(n+\frac{1}{2}\right)^2\pi^2+(2kh)^2}\left(2kh\tanh(2kh)+\frac{(-1)^n\left(n+\frac{1}{2}\right)\pi}{\cosh(2kh)}\right)\right]\end{aligned} \tag{18}$$

and

$$\frac{\overline{\overline{U}}_{E,\,\mathrm{steady}}(z/h)}{U_S(z=0)} = \frac{\tanh(2kh)}{\sqrt{2iEk^{-1}}}\frac{\sinh\left(2kh\sqrt{2iEk^{-1}}\,(1+z/h)\right)}{\cosh\left(2kh\sqrt{2iEk^{-1}}\right)}\left(1-\frac{2iEk^{-1}}{1-2iEk^{-1}}\right)$$
$$+\frac{1}{\cosh(2kh)}\frac{\cosh\left(2kh\sqrt{2iEk^{-1}}\,z/h\right)}{\cosh\left(2kh\sqrt{2iEk^{-1}}\right)}\left(\frac{3}{2}-\frac{2iEk^{-1}}{1-2iEk^{-1}}\right)$$
$$+\frac{\cosh(2kh(1+z/h))}{\cosh(2kh)}\left(\frac{1}{1-2iEk^{-1}}-1\right) \tag{19}$$

where the latter $\left(\overline{\overline{U}}_{E,\,\mathrm{steady}}(z/h)\right)$ corresponds to the solution to the steady (time-independent) version of Equation 4, where $\overline{\overline{\{\}}}$ indicates an average over both wave and inertial time scales. The same solution for the Eulerian-mean velocity can be found by taking the Laplace transform of Equations 4, 5, and 6 for the Stokes drift given in Equation 16, solving the resulting ODE in Laplace space and calculating the inverse Laplace transform by using a contour integral and Cauchy's residue theorem (see Texts S2 and S3 in Supporting Information S1). The steady solution $\overline{\overline{U}}_{E,\,\mathrm{steady}}(z)$ is equal to the steady solution given by Xu and Bowen (1994), when considering only the wave-driven flow outside the bottom boundary layer. Xu and Bowen (1994) also consider the unsteady flow driven by a suddenly imposed constant wave forcing, but do not provide a fully explicit solution. However, explicitly calculating the integral expression they give (equation 100 Xu & Bowen, 1994) leads to Equation 17 (see Appendix A).

To assess the range of Ek^{-1} for realistic conditions near the coast, we explore buoy measurements of the wave conditions along the coastlines of the United States provided by the Coastal Data Information Program (CDIP). We gather all historic data (containing 187 buoy stations) and select the measurements for which $kh < 3$ (estimated based on the water depth and the recorded peak wave period). For this data set of coastal wave conditions, the peak wave period is between 3 and 25 s, with a mean of 11 s. Based on the water depth, latitude and the recorded peak period, and assuming an eddy viscosity of $\nu = 10^{-3}$ m^2 s^{-1}, we find (inverse) wave Ekman numbers between 0.05 and 356, with a mean of 9. Of the estimated (inverse) wave Ekman numbers 95% are in the range $0 < Ek^{-1} < 30$ and only 0.13% are larger than 100. In the figures in this paper we, therefore, show the typical values $Ek^{-1} = 5, 10, 30$ (corresponding to, e.g., a wave with a period between 10 and 15 s, a mid latitude value of the Coriolis parameter $f = 1 \times 10^{-4}$ rad/s, $\nu = 10^{-3}$ m^2/s and $kh = 1.5$) and the less common value $Ek^{-1} = 100$. However, the value of Ek^{-1} critically depends on the value of the eddy viscosity, where a higher value of the eddy viscosity leads to a lower (inverse) wave Ekman number (and vice versa). In the open ocean, the eddy viscosity is estimated to be of the order of 10^{-3}–10^{-2} (Cunningham et al., 2022). Cunningham et al. (2022) calculated this by using the Mellor and Yamada (1982) 2.5 level turbulence model, which relates the eddy viscosity to the turbulent kinetic energy and the turbulent length scale, together with the vertical mixing coefficient from Mellor and Blumberg (2004). Near the coast, the eddy viscosity might vary over several orders of magnitude with estimates in the range of 10^{-4}–10^{-2} (Cao et al., 2017; Geyer & MacCready, 2014; Sentchev et al., 2023; Yoshikawa & Endoh, 2015). However, due to the difficulty of determining the eddy viscosity, which is dependent on the local sea state, the uncertainties in these estimates are large.

The steady solution (Equation 19) is shown in Figure 2 as a function of depth for different values of kh and (inverse) wave Ekman number. As noted by Xu and Bowen (1994), rotation causes the flow to be contained in two Ekman layers, one near the surface driven by the (virtual tangential) wave stress and one near the bottom driven by the bottom streaming (see Figures 2b–2e). For $kh = 3$, we approach the deep-water solution in which only the surface Ekman layer remains (Figures 2c–2f). While Xu and Bowen (1994) plot only a single case (one value of kh and Ek^{-1}), Figure 2 demonstrates the effect of kh and Ek^{-1} on the velocity profile by showing a range of values. An increase in either kh (deeper water) or Ek^{-1} (larger relative effect of rotation) leads to a reduction of the Lagrangian drift velocity in the central region of the water column, as well as a decrease in the thickness (compared to the water depth) of the bottom and surface Ekman layers, as can be seen from the $\sinh\left(2kh\sqrt{2iEk^{-1}}\,(1+z/h)\right)$ and $\cosh\left(2kh\sqrt{2iEk^{-1}}\,z/h\right)$ terms in Equation 19. Laboratory experiments measuring the surface drift induced by

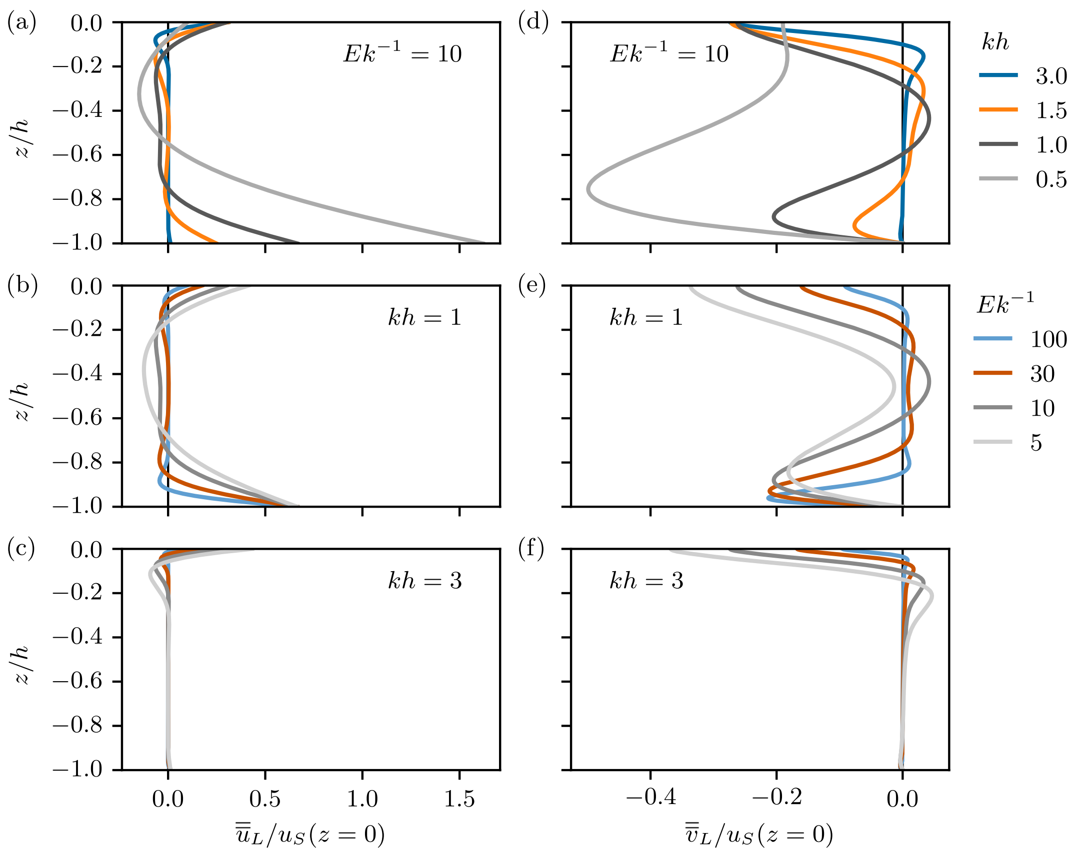

Figure 2. The steady Lagrangian-mean velocity normalized by the Stokes drift at the surface $\overline{\overline{U}}_{L,\,\mathrm{steady}}(z)/U_S(z=0) = \left(\overline{\overline{U}}_{E,\,\mathrm{steady}}(z) + U_S(z)\right)/U_S(z=0)$ as a function of the vertical coordinate for waves in the x-direction, such that $U_S = u_S$, and different values of kh and Ek^{-1}. The left column (a–c) shows the velocity in the x-direction and the right column (d–f) shows the velocity in the y-direction.

deep-water waves under rotation have already shown that an increase in rotation rate reduces the mean Lagrangian drift (Mol et al., 2025). Figure 2b and (e) illustrate that a reduction in the drift velocity due to an increase in the rotation rate (larger Ek^{-1}) is also expected to occur for finite-depth waves, both at the surface and at depth. The cancellation is generally expected to be less complete for finite depth, mostly due to the important role of bottom boundary layer streaming.

The time-dependent Eulerian-mean velocity for a suddenly imposed constant wave field (Equation 17) is given in Figure 3. Both the $\overline{u}_E$ and $\overline{v}_E$ velocity consist of damped inertial oscillations around the value given by the steady solution (Equation 19). Although Figure 3 only shows the velocities at the surface, these inertial oscillations occur throughout the water column with time- and z-dependent amplitudes (see Equation 17). A decrease in either kh (shallower water) or Ek^{-1} (smaller effect of rotation compared to viscosity) causes the inertial oscillations to decay faster. Examining Equation 17 shows that the $\exp(-i\tau)$ term drives the inertial oscillations and the $\exp\left(-\left(n+\frac{1}{2}\right)^2\pi^2\tau/\left(2Ek^{-1}(2kh)^2\right)\right)$ terms are responsible for the damping. Since we have a sum of these exponential terms, the oscillations do not show a single exponential decay. To still quantify the decay of the inertial oscillations, we examine the envelope of the oscillations (the time-dependent part of Equation 17, but without the oscillating $\exp(-i\tau)$ term) defined as

$$I(z/h,\tau) = e^{i\tau}\left(\frac{\overline{U}_E(z/h,\tau)}{U_S(z=0)} - \frac{\overline{\overline{U}}_{E,\,\mathrm{steady}}(z/h)}{U_S(z=0)}\right). \tag{20}$$

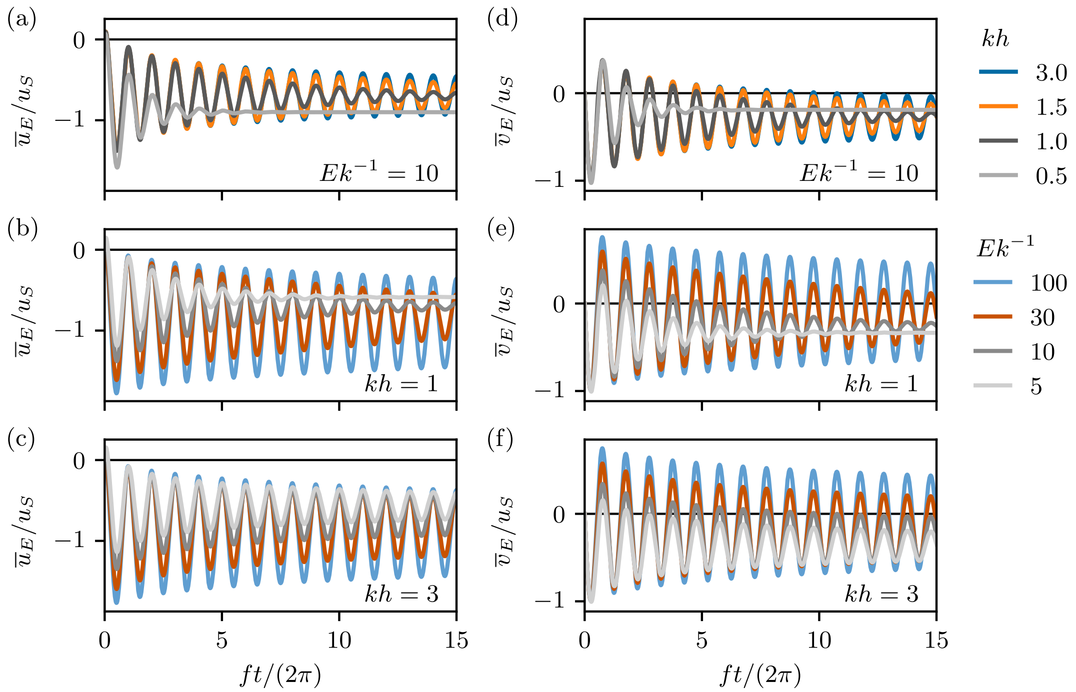

Figure 3. The Eulerian-mean velocity $\overline{U}_{E,\mathrm{const}}(z/h, \tau)/U_S(z = 0)$ as a function of time for a suddenly imposed constant wave forcing in the x-direction, such that $U_S(z = 0) = u_S$, for $z/h = 0$ and different values of kh and Ek^{-1}. The time is shown in number of inertial periods. The left column (a–c) shows the velocity in the x-direction and the right column (d–f) shows the velocity in the y-direction.

We calculate the half-life time and the analogous quarter-life time of the oscillations by determining when the envelope $I(z/h, \tau)$ reaches half of its maximum value and a quarter of its maximum value. The resulting life times are shown in Figure 4. The half-life time and the quarter-life time both show a strong dependence on the (inverse) wave Ekman number, where a lower value of Ek^{-1} (less relative importance of rotation and more relative importance of viscosity) leads to shorter life times (faster decay of the oscillations). A decrease in water depth also leads to a reduction in the life times. For the quarter-life time this effect of the water depth starts to occur at the transition between the deep-water regime and the finite-depth regime ($kh \approx 3$), while the half-life time is only influenced by small values of kh. Figure 4, therefore, demonstrates that while kh and Ek^{-1} have a similar effect on the life times of the inertial oscillations, it is ultimately the combination that determines the behavior of the flow. We also notice that the quarter-life time is much longer then twice the half-life time. This means that the oscillations quickly reduce in amplitude, but that it takes much longer for them to disappear.

4.2. Exponential Attenuation

We will now consider the solution for a simple (exponentially decaying) time dependence of the forcing and evaluate the flow after the forcing has dissipated. Since the boundary conditions of Longuet-Higgins (1953) assume a free surface without any normal wind stress, there is no explicit wave growth mechanism included in our model (see also Section 6). We therefore also consider the case of (viscous) exponential attenuation of the suddenly imposed wave forcing with a Stokes drift of

$$U_{S,\mathrm{atten}}(z, t) = \begin{cases} 0 & t < 0, \\ U_S(z)\, e^{-2\beta t} & t \geq 0, \end{cases} \tag{21}$$

where β is the attenuation coefficient of the wave amplitude. Calculation of the convolution (Equation 11) of the Stokes drift (Equation 21) with the finite-depth Ekman–Stokes kernel gives (see Text S3 in Supporting Information S1)

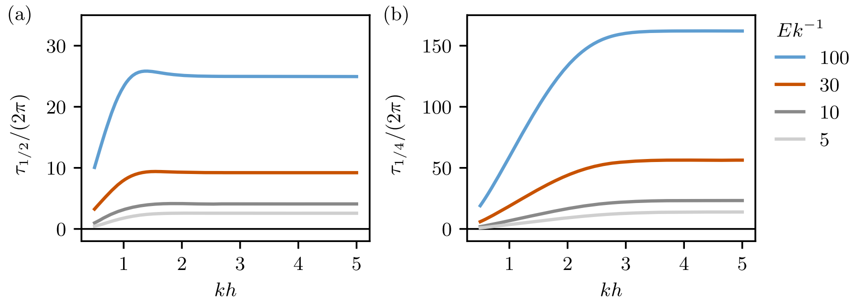

Figure 4. The half-life time in number of inertial periods $\tau_{1/2}/(2\pi)$ (a) and the quarter-life time in number of inertial periods $\tau_{1/4}/(2\pi)$ (b) of the envelope of the inertial oscillations (Equation 20) in the Eulerian-mean velocity for a suddenly imposed constant forcing in the x-direction $\overline{U}_{E,\mathrm{const}}(z/h,\tau)/U_S(z=0)$ as a function of kh for different values of Ek^{-1} at $z=0$.

$$\frac{\overline{U}_{E,\mathrm{atten}}(z/h,\tau)}{U_S(z=0)} = e^{-i\tau}\sum_{n=0}^{\infty} e^{-\left(n+\frac{1}{2}\right)^2\pi^2\tau/\left(2Ek^{-1}(2kh)^2\right)}\,\mathcal{F}_{n,\mathrm{atten}}\cos\left(\left(n+\frac{1}{2}\right)\pi\frac{z}{h}\right) + e^{-(2\beta/f)\tau}\,\mathcal{G} \tag{22}$$

with

$$\begin{aligned}\mathcal{F}_{n,\mathrm{atten}} = {} & \frac{1}{1+2i\beta/f+\left(n+\frac{1}{2}\right)^2\pi^2/\left(2iEk^{-1}(2kh)^2\right)} \\ & \times\left[\frac{-2}{2iEk^{-1}(2kh)^2}\left(2kh\tanh(2kh)+\frac{3}{2}\frac{(-1)^n\left(n+\frac{1}{2}\right)\pi}{\cosh(2kh)}\right)\right. \\ & \left.+\frac{2}{\left(n+\frac{1}{2}\right)^2\pi^2+(2kh)^2}\left(2kh\tanh(2kh)+\frac{(-1)^n\left(n+\frac{1}{2}\right)\pi}{\cosh(2kh)}\right)\right]\end{aligned} \tag{23}$$

and

$$\begin{aligned}\mathcal{G} = {} & \frac{\tanh(2kh)}{\sqrt{2iEk^{-1}(1+2i\beta/f)}}\frac{\sinh\left(2kh\sqrt{2iEk^{-1}(1+2i\beta/f)}\,(1+z/h)\right)}{\cosh\left(2kh\sqrt{2iEk^{-1}(1+2i\beta/f)}\right)} \\ & \times\left(1-\frac{2iEk^{-1}}{1-2iEk^{-1}(1+2i\beta/f)}\right)+\frac{1}{\cosh(2kh)}\frac{\cosh\left(2kh\sqrt{2iEk^{-1}(1+2i\beta/f)}\,z/h\right)}{\cosh\left(2kh\sqrt{2iEk^{-1}(1+2i\beta/f)}\right)} \\ & \times\left(\frac{3}{2}-\frac{2iEk^{-1}}{1-2iEk^{-1}(1+2i\beta/f)}\right)+\frac{\cosh(2kh(1+z/h))}{\cosh(2kh)}\left(\frac{1-2iEk^{-1}2i\beta/f}{1-2iEk^{-1}(1+2i\beta/f)}-1\right).\end{aligned} \tag{24}$$

The same expression can be obtained by solving Equation 4 for a suddenly imposed exponentially attenuating Stokes drift (Equation 21) using Laplace transforms (see Text S3 in Supporting Information S1). For an attenuation coefficient of $\beta = 0$, the solution reduces to the solution for a suddenly imposed constant wave field (Equation 17).

Figure 5 shows the Eulerian-mean velocity forced by a suddenly imposed viscously attenuated wave field for different values of kh and Ek^{-1}. The viscous attenuation of the wave forcing (Equation 21) is given by $\exp(-(2\beta/f)\tau)$ in non-dimensional form. For deep water, the viscous dissipation occurs due to internal friction gives (Phillips, 1977)

$$\frac{\beta_{\mathrm{deep}}}{f} = \frac{2\nu k^2}{f} = \frac{1}{4\,Ek^{-1}}. \tag{25}$$

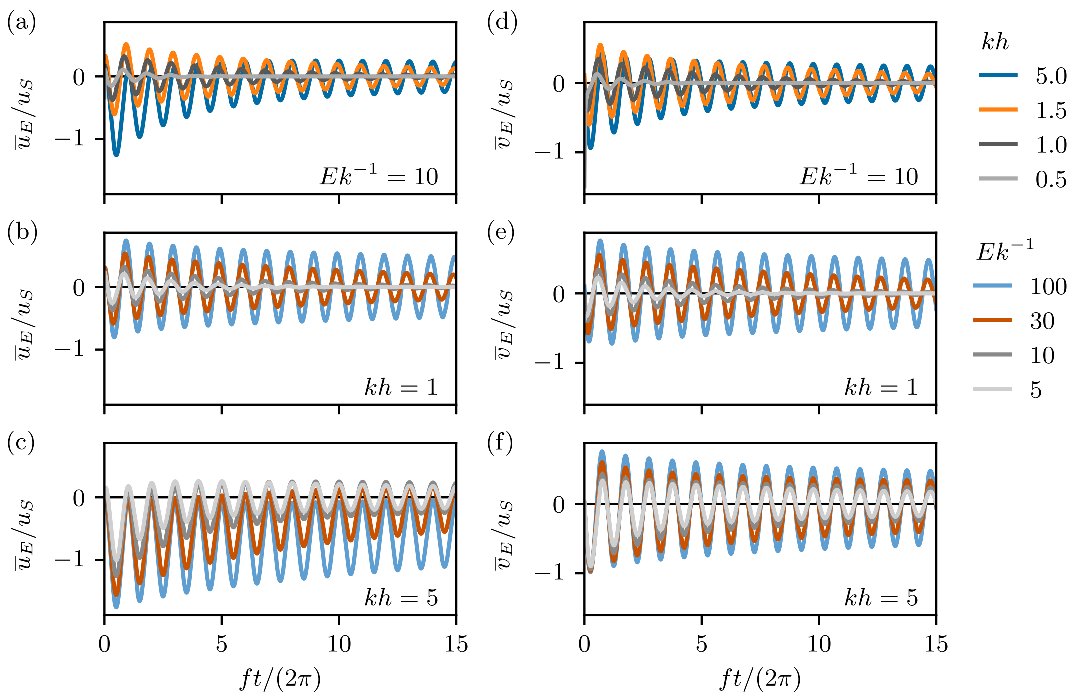

Figure 5. The Eulerian-mean velocity $\overline{U}_{E,\text{atten}}(z/h, \tau)/U_S(z = 0)$ as a function of time for a suddenly imposed exponentially attenuated wave forcing in the x-direction, such that $U_S(z = 0) = u_S$, for $z/h = 0$ and different values of kh and Ek^{-1}. For deep water ($kh = 5$), we use β_{deep}, and for finite depth ($kh = 0.5, 1.0, 1.5$), we use β_{finite}, where we estimate $\sqrt{\omega/f}$ based on $f = 1 \times 10^{-4}$ rad/s and a wave period of $T = 10$ s. This gives a half-life time $\tau_{1/2}$ of the forcing of 0.01–0.1 inertial periods for finite depth and 1 to 22 inertial periods for deep water. The time is shown in number of inertial periods. The left column (a–c) shows the velocity in the x-direction and the right column (d–f) shows the velocity in the y-direction.

In shallow and intermediate water depths, the dissipation due to friction at the bottom boundary dominates and gives (Phillips, 1977)

$$\frac{\beta_{\text{finite}}}{f} = \frac{1}{f}\frac{\nu k}{\delta_\nu \sinh(2kh)} = \frac{\sqrt{\omega/f}}{4\sqrt{Ek^{-1}}\sinh(2kh)}. \tag{26}$$

These attenuation coefficients cause a rapid decrease in the wave forcing, especially for finite depth. In Figure 5, the forcing has a half-life time of 1–22 inertial periods for deep water and 0.01 to 0.1 inertial periods for finite depth (see also Figure S3 in the Supporting Information S1). The resulting $\overline{u}_E$ and $\overline{v}_E$ velocities again consist of inertial oscillations, which disappear faster for lower values of kh and Ek^{-1}. However, as soon as the forcing has attenuated, both velocities oscillate around zero (Figure 5), rather than around a non-zero steady solution, as is the case for a suddenly imposed constant forcing (Figure 3). This illustrates that the (oscillatory) Eulerian-mean velocities remain, even when there is no longer any wave forcing (see also Figure 1 in Weber, 1983a), while the value around which they oscillate depends on the forcing that is active at that time. The reason for this is that the time scale of orbital motion of the waves is much shorter than the time scale of inertial oscillations ($1/\omega \ll 1/f$). Inertial oscillations observed in a coastal sea might, therefore, be from a past storm, where the associated wave field has already decayed (see also Section 5.1).

5. Application to Realistic Forcing Conditions

5.1. Gaussian Storm

In realistic ocean conditions the wave forcing is not suddenly imposed, but typically has a more gradual time variation. To illustrate the effect of such a time dependence we consider an idealized Gaussian storm with a Stokes drift at the surface of

10.1029/2026JC024014

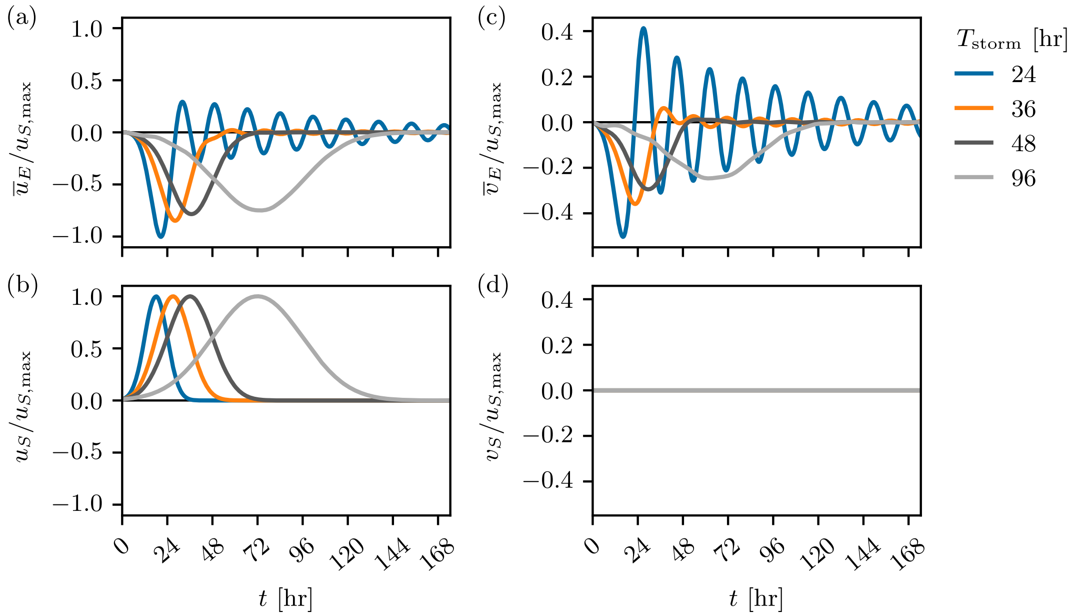

Figure 6. The Eulerian-mean velocity (a, c), given by Equation 11, generated by a Gaussian storm (b, d), given by Equation 27, as a function of time for different storm durations $T_{\text{storm}} = 4\sigma$ with $z/h = 0$, $kh = 1$, $f = 1 \times 10^{-4}$ rad/s, $Ek^{-1} = 10$ and $t_{\max} = 3\sigma$. The left column (a, b) shows the velocity in the x-direction and the right column (c, d) shows the velocity in the y-direction.

$$U_S(t) = u_{S,\max}\, e^{-(t-t_{\max})^2/(2\sigma^2)}, \tag{27}$$

where σ is the standard deviation, which controls the duration of the storm, and the maximum value $u_{S,\max}$ is reached at $t_{\max}$. The Eulerian-mean velocity resulting from the convolution of the finite-depth Ekman–Stokes kernel with a Gaussian storm is shown in Figure 6 for different storm durations. For a Gaussian curve, 95% of the area lies within $t_{\max} \pm 2\sigma$, such that we consider the storm duration to be given by $T_{\text{storm}} = 4\sigma$ (note that here we use the standard deviation of the Stokes drift and that the standard deviation of the wave height differs by a factor of $\sqrt{2}$). The global coastal mean duration of wave storms is in the range of 24–120 hr, where for most locations the mean duration lies between 24 and 72 hr (Lobeto et al., 2024). Hence, the selected storm durations in Figure 6 of $T_{\text{storm}} = 24$ hr ($\sigma = 6$ hr) to $T_{\text{storm}} = 96$ hr ($\sigma = 24$ hr) are representative of realistic conditions. Figure 6 shows a combination of the effects previously observed for a suddenly imposed constant wave forcing (Section 4.1) and for a suddenly imposed attenuated wave forcing (Section 4.2). Namely, the storm with a duration of $T_{\text{storm}} = 24$ hr shows decaying inertial oscillations, like in Figure 3 (constant wave field), and it shows oscillations around zero after the forcing has disappeared, like in Figure 5 (attenuated forcing). Accordingly, field observations of inertial oscillations could, therefore, be caused by a past storm event with a fast time variation. The Eulerian-mean velocity $\overline{u}_E$ (Figure 6a) follows the forcing velocity u_S (Figure 6b) quite closely for the duration of each of the storms, but with an opposite sign. However, the response in $\overline{u}_E$ after the storm has passed and the response in $\overline{v}_E$ (Figure 6c) are both very dependent on the duration of the storm. A shorter storm with a faster onset (and a faster decay) causes much more prominent inertial oscillations then a longer storm with a slower time variation. It is this time variation that controls the generation of the inertial oscillations, where a faster time variation in the arrival of the storm creates oscillations with a larger amplitude (see Figure S4 in the Supporting Information S1). The time variation (and associated duration) of a storm is, therefore, crucial for the resulting wave-induced flow.

5.2. Buoy Data

To demonstrate the use of finite-depth kernel for real sea conditions, we obtain buoy data from the Coastal Data Information Program (CDIP). The Imperial Beach Nearshore buoy, located near the coast of San Diego in water with a depth of 21 m (32.57°N, 117.17°W), provides observational data of the significant wave height $H_S(t)$, peak period $T_p(t)$ and peak direction $D_p(t)$ with a half hour resolution. Based on this data we estimate the Stokes drift by

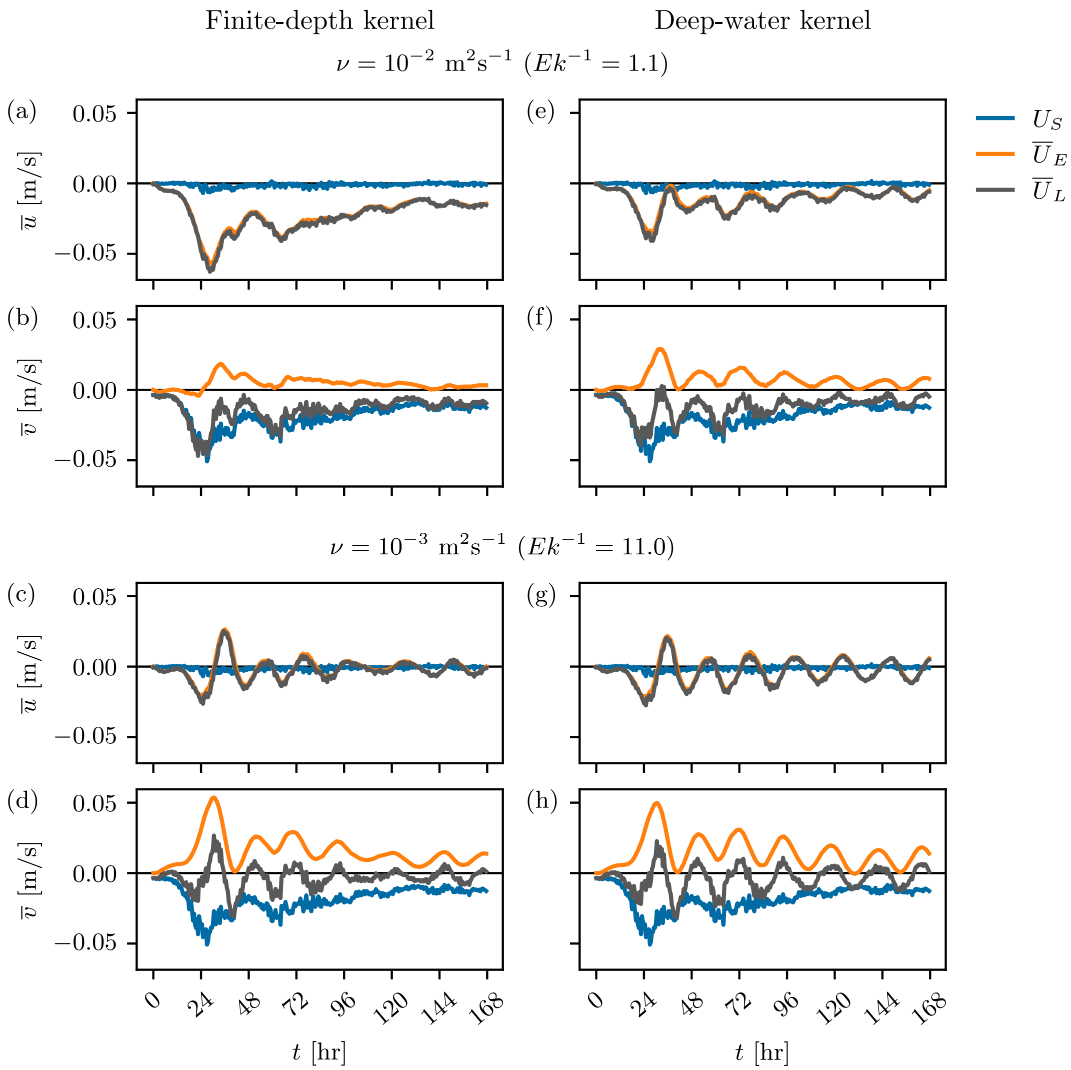

Figure 7. The wave-induced Eulerian-mean and Lagrangian-mean velocities at the surface computed using data from the Imperial Beach Nearshore buoy (32.57°N, 117.17°W) between the 22nd and the 29th of December 2024, for which $kh = 0.6$ and $f = 2\Omega \sin(\phi) = 0.8 \times 10^{-4}$ rad/s with ϕ the latitude of the buoy and Ω the rotation rate of the Earth. The left column (a–d) shows the velocities calculated from the convolution (Equation 11) of the Stokes drift (Equation 28) with the finite-depth kernel (Equation 13). The right column (e–h) shows the deep-water equivalent, where we have used the same (finite-depth) Stokes drift, but applied the deep-water kernel of Higgins et al. (2020) instead. The top two rows (a, b, e, and f) assume an eddy viscosity of $\nu = 10^{-2}$ m^{2}s^{-1}, giving $Ek^{-1} = 1.1$, while the bottom two rows (c, d, g, and h) assume $\nu = 10^{-3}$ m^{2}s^{-1}, giving $Ek^{-1} = 11$.

$$U_S(z,t) = a^2(t)\omega k \frac{\cosh(2k(h+z))}{2\sinh^2(kh)} e^{i\theta(t)}, \tag{28}$$

with $a(t) = H_S(t)/(2\sqrt{2})$, $\theta(t) = D_p(t) * \pi/180$, $\omega = \langle 2\pi/T_p(t)\rangle$ and $k = \langle k_p(t)\rangle$ with the peak wavenumber $k_p(t)$ calculated from the linear dispersion relation based on $T_p(t)$ and h, where $\langle\rangle$ denotes taking the mean over the full selected record duration.

The estimated Stokes drift is shown in Figure 7, together with the resulting Eulerian-mean and Lagrangian-mean velocities calculated using the finite-depth kernel and the deep-water kernel of Higgins et al. (2020). The corresponding trajectories are shown in Figure 8. In calculations with the deep-water kernel, we use the same (finite-depth) estimate of the Stokes drift based on Equation 28, since the effect of using the deep-water limit of Equation 28 would dominate the comparison with finite depth and obscure the effect of using a different kernel.

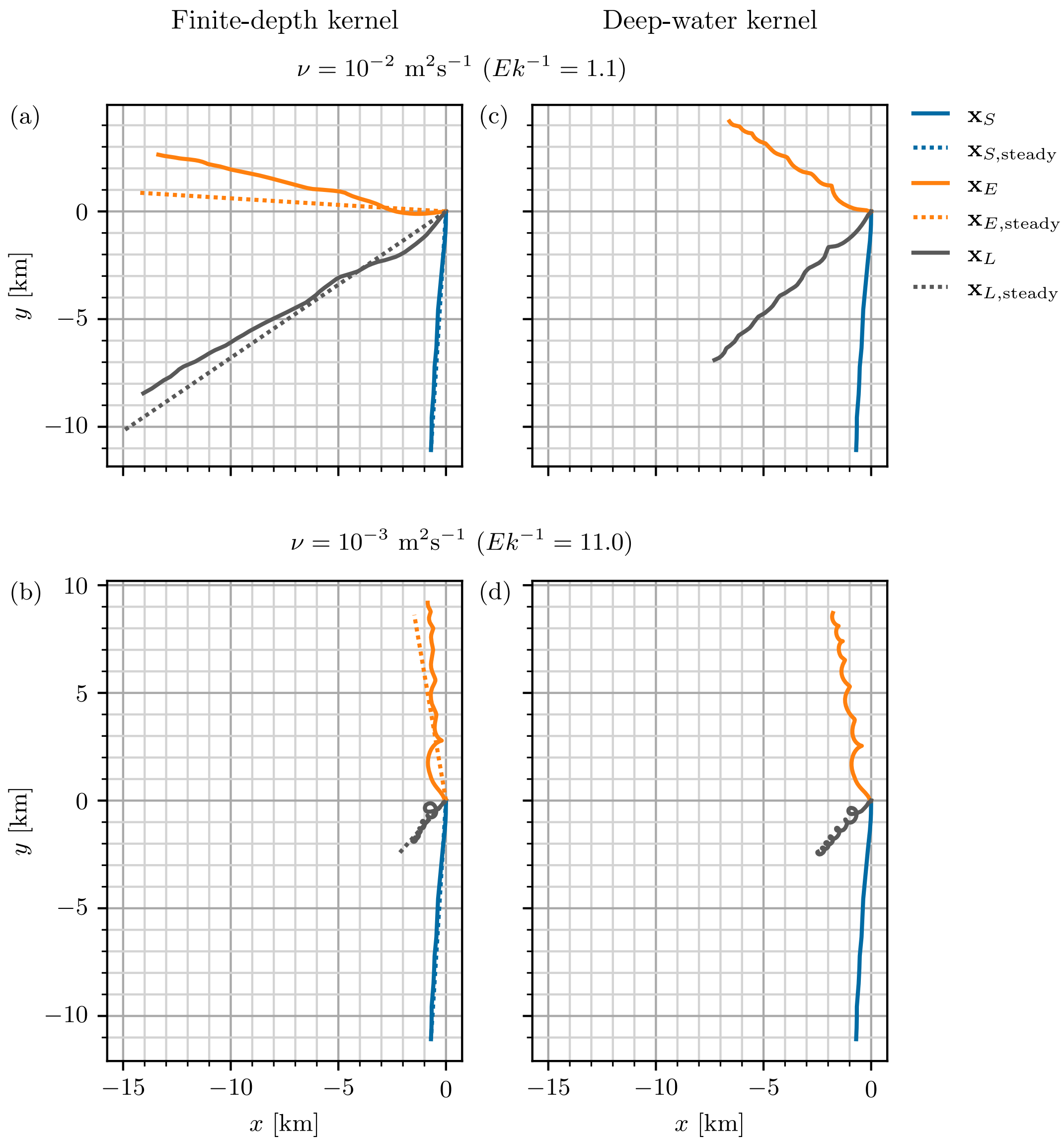

Figure 8. The surface trajectories computed using data from the Imperial Beach Nearshore buoy (32.57°N, 117.17°W) between the 22nd and the 29th of December 2024, for which $kh = 0.6$ and $f = 2\Omega \sin(\phi) = 0.8 \times 10^{-4}$ rad/s with ϕ the latitude of the buoy and Ω the rotation rate of the Earth. The trajectories correspond to the velocities shown in Figure 7. The left column shows the trajectories calculated using the estimated Stokes drift (Equation 28) and the finite-depth kernel (Equation 13) in solid lines and the steady trajectories, that ignore all time dependence, in dashed lines, where $\mathbf{x}_{S,\mathrm{steady}} = t\langle U_S \rangle$, $\mathbf{x}_{E,\mathrm{steady}} = t\overline{\overline{U}}_{E,\mathrm{steady}}$ and $\mathbf{x}_{L,\mathrm{steady}} = t\overline{\overline{U}}_{E,\mathrm{steady}} + t\langle U_S \rangle$ with the angular brackets denoting averaging over the full duration shown (and $\overline{\overline{U}}_{E,\mathrm{steady}}$ computed using this averaged value of U_S). The right column shows the deep water equivalent, where we used the same Stokes drift, but applied the Higgins et al. (2020) deep-water kernel instead. All tracks start at the origin (0,0). The top row (a, c) assumes an eddy viscosity of $\nu = 10^{-2}$ m^{2}s^{-1}, giving $Ek^{-1} = 1.1$, while the bottom row (b, d) assumes $\nu = 10^{-3}$ m^{2}s^{-1}, giving $Ek^{-1} = 11$.

For the selected record duration of the 22nd to the 29th of December 2024, we find a relative water depth of $kh = 0.6$. The peak wave direction is in the negative y-direction, which is directed toward the coast, giving a negative v_S and a near-zero u_S. For the lower value of the eddy viscosity (higher Ek^{-1}) used in Figures 7c and 7d), we observe inertial oscillations, in contrast to Figures 7a and 7b) where a higher value of the eddy viscosity (lower Ek^{-1}) was used. The value of the eddy viscosity is therefore key, since it determines the behavior of the resulting flow through a different value of the (inverse) wave Ekman number. When we compare the velocities in Figures 7a and 7b to 7e and 7f, we notice that for this higher value of the eddy viscosity (lower Ek^{-1}) the Eulerian-

10.1029/2026JC024014

mean velocity calculated with the deep-water kernel shows inertial oscillations, while the finite-depth kernel does not predict these. This shows the importance of taking the water depth into account and emphasizes that it is the combination of kh and Ek^{-1} that ultimately determines the Lagrangian-mean velocity. In line with Sections 4.1 and 4.2, the difference between Figures 7c and 7d with 7g and 7h shows that the inertial oscillations decay faster in finite-depth water. Figures 7d–7h illustrates that a (rapid) increase in the Stokes drift magnitude can generate inertial oscillations and that these remain after the wave forcing has decreased, which is in accordance with observations in Section 5.1. Observed inertial oscillations can, therefore, be caused by a past wave event with a larger wave height and faster time variation (compared to the current conditions).

The effects described above can also be seen in Figure 8 when comparing the trajectories for different viscosity values and when comparing the trajectories predicted by the finite-depth and deep-water kernels. A Lagrangian tracer particle does not travel with the Stokes drift alone, but is transported to the right of the Stokes drift direction with the Lagrangian-mean velocity, due to the addition of the wave-induced Eulerian-mean velocity. For deep water, it has already been demonstrated that taking this Eulerian-mean velocity into account leads to a considerable change in the predicted trajectory (Cunningham et al., 2022; Higgins et al., 2020). Figure 8 shows that this is also the case in finite-depth water. The wave-induced Eulerian-mean velocity can largely cancel the Stokes drift (anti-Stokes flow), depending on the value of the eddy viscosity (resulting in different values of Ek^{-1}).

Using the mean of the estimated Stokes drift (Equation 28) and the steady solution (Equation 19), the time-independent response is shown in Figures 8a and 8b with dashed lines. This steady approximation does not resolve the inertial oscillations, but provides reasonable agreement with the finite-depth kernel for the net transport over the full duration shown (1 week). Comparing $\mathbf{x}_L$ with $\mathbf{x}_{L,\text{steady}}$ yields a root mean square error (RMSE) in the predicted distance from the initial position over a 1-week period of 0.9 km $\left(Ek^{-1} = 1.1\right)$ and 0.4 km $\left(Ek^{-1} = 11.0\right)$, corresponding to 5% and 11%, respectively, of the length of the trajectory predicted by the steady approximation. At early times, the relative error is substantially larger (see Figure S5 in the Supporting Information S1). For $Ek^{-1} = 1.1$, the RMSE in the predicted distance ranges from 35% to 62% of the time-independent prediction during the first 24 hr. For $Ek^{-1} = 11.0$, this relative error is between 17% and 36% during the first 48 hr of the trajectory. Including the time-dependence of the flow can therefore be essential for accurate transport predictions at early times but is of limited importance on longer time-scales. Furthermore, the RMSE in the transport in the (negative) y-direction, which is closely aligned with the mean wave direction, is generally smaller than the RMSE in the transport in the x-direction. It should be noted that the calculation of the convolution of the Stokes drift with the kernel is sensitive to the time resolution, while the steady approximation is independent of this. However, in this case, we are limited by the discrete nature of the buoy data (30-min resolution).

Comparing Figures 8a and 8c, shows that using the finite-depth kernel instead of the deep-water kernel can lead to a substantial difference in the predicted surface transport. For $Ek^{-1} = 1.1$, the net displacement increases by 64% in finite depth compared to deep water, whereas for $Ek^{-1} = 11.0$ a decrease of 29% is observed. In practical applications, the vertically integrated transport in the near-surface region often provides a more robust measure than the drift at a specific depth (as is the case for Ekman spirals, cf. Lenn and Chereskin (2009)). The impact of finite depth on the vertically integrated transport is considerably larger than on the surface displacement, due to the difference in the vertical structure of the flow. The vertically integrated Lagrangian transport over the Stokes depth (from $z = -1/(2k)$ to $z = 0$) is more than twice as large when using the finite-depth kernel as opposed to the deep-water approximation (see Figure S6 in the Supporting Information S1).

6. Discussion and Conclusion

In this paper, we have presented a model for the time-dependent wave-induced drift in finite-depth water including the effect of both rotation and a constant eddy viscosity. We provide the solution for a general time dependence of the wave forcing in the form of the finite-depth Ekman–Stokes kernel. The convolution of any given time series of the Stokes drift forcing (e.g., estimated from observations) with the finite-depth kernel gives the generated wave-induced Eulerian-mean velocity. As such, the kernel is readily applied in particle tracking simulations, as was done by Cunningham et al. (2022) for the deep-water kernel by Higgins et al. (2020). Solutions for the Eulerian-mean velocity induced by a suddenly imposed constant wave forcing and a suddenly imposed viscously attenuated wave forcing are also given. Our solutions recover the solutions by Xu and Bowen (1994) if the integral therein is explicitly evaluated.

10.1029/2026JC024014

The assumption of a constant eddy viscosity likely breaks down for realistic coastal conditions. A different eddy viscosity profile could modify the wave-induced drift velocity (Lentz, 1995; Weber, 2019). Future work should extend the model by allowing a depth dependence of the eddy viscosity, such as a linear variation with depth (Lewis & Belcher, 2004; Polton et al., 2005). We note that the turbulence model has several roles: it affects the linear surface gravity waves, their decay rate and, consequently, the virtual wave stress, but it also sets the vertical structure of the mean flow and the damping of inertial oscillations contained therein. When comparing to field data, which aspect the comparison will be focused on will matter for choosing the right turbulence model. Even a linearly varying eddy viscosity would probably be insufficient to capture the full complexity of the turbulent mixed layer in coastal seas, due to the presence of a wide range of processes, including Langmuir circulation (Gargett et al., 2004; Kukulka et al., 2012) and, closer to the shore, the vertical mixing resulting from wave breaking (Reniers et al., 2004). We envisage that increasing the complexity of the model, for example, by introducing a multi-equation turbulence model, would reduce its tractability and primarily affect the vertical structure of the flow, while leaving the underlying mechanisms unchanged and only influencing the solution quantitatively. Furthermore, the question whether using an eddy viscosity model (both the model itself and the high vales of eddy viscosity of $10^{-3} - 10^{-2}$ m^2 s^{-1} chosen to parameterize vertical mixing) is appropriate for calculating the virtual wave stress, as we have done here, is not limited to its vertical dependence. Eddy viscosities as high as those used in the present study are likely to damp the waves too quickly compared to field observations (e.g., Ardhuin & Jenkins, 2006). Explicitly modeling the production of turbulent kinetic energy, as in Ardhuin and Jenkins (2006), can potentially give quantitatively correct estimates of both wave damping and vertical mixing as relevant for drift.

For wind-driven Ekman spirals, the depth dependence of the eddy viscosity is a key factor underlying the discrepancy between the classical Ekman spiral and observations (Lenn & Chereskin, 2009). As a result, the Ekman transport (the vertically integrated Ekman velocity) is often more reliably predicted than the vertical structure of the velocities. For comparison with observations, the present model can, therefore, also be used to estimate the vertically integrated transport. We provide the solutions for a quasi-monochromatic wave field. This will make the application to long-duration forcing with a changing peak frequency challenging. An extension that takes the broad-banded nature of realistic wave fields into account may be necessary to capture a realistic depth variation of the forcing to be used in combination with a different turbulence model. Further complexity may be incorporated by including spatial variations in both the wave field and bottom topography, as well as by accounting for the effects of stratification, which could modify the damping of inertial oscillations (Bell, 1978), which are now set to decay due to viscous dissipation alone. The latter assumption may yield decay rates of our inertial response that are not realistic. Additionally, our model does not include a wave growth/decay mechanism.

When using a Lagrangian rather than a Eulerian framework, the wave-averaged equations can also be solved inside the surface boundary layer (Weber, 1983a, 1983b), without the need for a curvi-linear coordinate transformation. This allows for the inclusion of a coupling between the surface stress and the wave growth/decay rate. Weber (1983b) shows that an oscillating normal stress at the surface can exactly compensate the viscous decay of the wave amplitude. Weber (2019) derives the relation between the normal stress at the surface and the temporal and spacial decay rates for finite-depth and deep water. Analogous to the derivation of Jenkins (1986) for deep water, the result by Weber (2019) can be used to extend our model by deriving the wave-averaged Lagrangian-mean velocity for a given surface stress and corresponding time-dependence of the wave forcing. The velocities inside and just below the surface boundary layer, which are affected by the coupling between the wind and waves, are essential in determining the transport of floating marine litter and other materials near the surface. A better understanding of this air-water interface could, therefore, improve transport predictions in this surface region.

The combined effect of rotation and viscosity leads to a non-zero inertially averaged steady Lagrangian-mean velocity, with a reduced magnitude compared to the Stokes drift, as previously shown by Xu and Bowen (1994). In finite-depth, rotation confines this steady flow to two Ekman layers (Figure 2), one at the surface driven by the (virtual tangential) wave stress and one at the bottom driven by the bottom streaming (Xu & Bowen, 1994). When we allow for time-variation of the wave-induced drift, the resulting Eulerian-mean velocity shows inertial oscillations. In finite-depth water with lower values of kh, these oscillations decay faster than in deeper water, as was shown for a suddenly imposed constant wave forcing (Figures 3 and 4), a suddenly imposed attenuated wave forcing (Figure 5) and a wave forcing time series estimated from buoy data (Figure 7). However, this decay is also influenced by the relative effect of rotation and viscosity given by (inverse) wave Ekman number $Ek^{-1} = f/(8\nu k^2)$. It is, therefore, the combination of kh and Ek^{-1} that determines the Lagrangian-mean velocity. Consequently, the value of the eddy viscosity is crucial, since it influences the value of Ek^{-1}. We have also shown that for an idealized Gaussian storm the Eulerian-mean response is dependent on the storm width, where a storm with a faster time variation leads to more prominent inertial oscillations. So altogether, it is the rate of change of the wave forcing that determines the strength of the inertial oscillations and the combination of kh and Ek^{-1} that controls how fast these oscillations decay. Hence, there are two aspects to the unsteadiness; the unsteadiness of the wave forcing and the unsteadiness of the resulting flow. For applications requiring short-term (1–2 days or less) forecasts, such as search-and-rescue or oil-spill modeling, accounting for the time variation of the flow can be crucial for accurate transport predictions, whereas for longer time-scale applications, such as plastic transport, the steady approximation may be sufficient. Taking the effect of finite depth into account can lead to a considerable difference in transport predictions, as illustrated by the comparison of the trajectories, and vertically integrated transport, calculated using the finite-depth kernel and the Higgins et al. (2020) deep-water kernel for CDIP buoy data (Figure 8). Particle tracking simulations near the coast should, therefore, include the effect of finite depth in order to make accurate predictions.

Appendix A: Comparison to Xu and Bowen (1994)

Xu and Bowen (1994) first consider the time-independent flow in the interior and bottom boundary layer, where they explicitly include the stress induced by the bottom friction and a wind stress at the surface. The steady solution they find for the wave-driven flow (without the effect of wind) is given by (their equation 78 written in our notation)

$$\overline{\overline{U}}_{E,\,\mathrm{XB\ steady}}(z) = \overline{\overline{U}}_{E,\,\mathrm{steady}}(z/h) + B(\gamma z'), \tag{A1}$$

with the contribution close to the bottom

$$\begin{aligned} B(\gamma z') = \frac{1}{2}U_S(z=-h)\big[e^{-2\gamma z'} - 2(\gamma z' + 2)\,e^{-\gamma z'}\cos(\gamma z') \\ - 2(\gamma z' - 1)\,e^{-\gamma z'}\sin(\gamma z')\big], \end{aligned} \tag{A2}$$

where $z' = z + h$ is the distance above the bottom, $\gamma = 1/\delta_\nu$ and $\overline{\overline{U}}_{E,\,\mathrm{steady}}(z/h)$ is given by Equation 19. They then examine the unsteady flow as a sum of this steady solution and a transient response to a suddenly imposed steady wave forcing. Rather than solving the full unsteady equations, they only solve for the transient response. Treating this as an eigenvalue problem in space, they find (Xu & Bowen, 1994, equation 100)

$$\overline{U}_{E,\,\mathrm{XB\ const}}(z,t) = \sum_{n=0}^{\infty} C_n e^{-ift} e^{-\left(n+\frac{1}{2}\right)^2\pi^2\nu t/h^2}\cos\left(\left(n+\frac{1}{2}\right)\pi\frac{z}{h}\right) + \overline{\overline{U}}_{E,\,\mathrm{XB\ steady}}(z), \tag{A3}$$

with

$$C_n = -\frac{2}{h}\int_{-h}^{0}\overline{\overline{U}}_{E,\,\mathrm{XB\ steady}}(z)\cos\left(\left(n+\frac{1}{2}\right)\pi\frac{z}{h}\right)\mathrm{d}z. \tag{A4}$$

Xu and Bowen (1994) explicitly state that they do not include further computation. When we calculate the integral for flow in the interior (excluding $B(\gamma z')$, which vanishes outside the bottom boundary layer) and rewrite the resulting expression in non-dimensional form, we find that Equation A3 is equal to Equation 17.

The flow resulting from an unsteady wave forcing is briefly explored by Xu and Bowen (1994) as a summation of incremental responses. The expression they provide is given by (Xu & Bowen, 1994, equation 110):

$$\overline{U}_{E,\,\mathrm{XB\ unsteady}}(z,t) = \int_0^t \frac{\mathrm{d}\zeta(T)}{\mathrm{d}t}\overline{U}_{E,\,\mathrm{XB\ const}}(z,t-T)\,\mathrm{d}T, \tag{A5}$$

where $\zeta(t)$ is the time dependence of the forcing such that $U_{S,\,\mathrm{XB}}(z,t) = U_S(z)\zeta(t)$. By rewriting this as a convolution, we find.

$$\overline{U}_{E,\,\mathrm{XB\ unsteady}}(z,t) = \frac{\mathrm{d}\zeta(t)}{\mathrm{d}t} * \overline{U}_{E,\,\mathrm{XB\ const}}(z,t) \tag{A6}$$

$$= \zeta(t) * \frac{\partial \overline{U}_{E,\,\mathrm{XB\ const}}(z,t)}{\partial t} \tag{A7}$$

$$= \int_0^t \zeta(T)\frac{\partial \overline{U}_{E,\,\mathrm{XB\ const}}(z,t-T)}{\partial t}\,\mathrm{d}T, \tag{A8}$$

where we have assumed that $\zeta(t = 0) = 0$. Calculating the time derivative of $\overline{U}_{E,\,\mathrm{XB\ const}}(z,t)$ for flow in the interior and writing $\overline{\overline{U}}_{E,\,\mathrm{steady}}(z/h)$ as a Fourier series (see Texts S2 and S3 in Supporting Information S1), we find that the expression is equal to the kernel solution (Equation 11).

Conflict of Interest

The authors declare no conflicts of interest relevant to this study.

Availability Statement

Buoy data was acquired from the Coastal Data Information Program (CDIP, 2026) and is publicly available at https://cdip.ucsd.edu. The Python code used to generate the figures in this publication is available at the 4TU. ResearchData repository: https://www.doi.org/10.4121/78d74e75-33b3-4db8-a2ba-61fdb93b8dc8.

Acknowledgments
The authors would like to thank Christopher Higgins for the helpful discussions on the derivations of the deep-water and finite-depth kernels.

References

Ardhuin, F., & Jenkins, A. D. (2006). On the interaction of surface waves and upper ocean turbulence. *Journal of Physical Oceanography*, *36*(3), 551–557. https://doi.org/10.1175/JPO2862.1

Bell, T. H. (1978). Radiation damping of inertial oscillations in the upper ocean. *Journal of Fluid Mechanics*, *88*(2), 289–308. https://doi.org/10.1017/S0022112078002116

Breivik, Ø., Mogensen, K., Bidlot, J.-R., Balmaseda, M. A., & Janssen, P. A. E. M. (2015). Surface wave effects in the NEMO ocean model: Forced and coupled experiments. *Journal of Geophysical Research: Oceans*, *120*(4), 2973–2992. https://doi.org/10.1002/2014JC010565

Cao, A.-Z., Chen, H., Fan, W., He, H.-L., Song, J.-B., & Zhang, J.-C. (2017). Estimation of eddy viscosity profile in the bottom Ekman boundary layer. *Journal of Atmospheric and Oceanic Technology*, *34*(10), 2163–2175. https://doi.org/10.1175/JTECH-D-17-0064.1

CDIP. (2026). Buoy observations of wave parameters [Dataset]. Scripps Institution of Oceanography, University of California. Retrieved from https://cdip.ucsd.edu

Craig, P. D., & Banner, M. L. (1994). Modeling wave-enhanced turbulence in the ocean surface layer. *Journal of Physical Oceanography*, *24*(12), 2546–2559. https://doi.org/10.1175/1520-0485(1994)024<2546:MWETIT>2.0.CO;2

Cunningham, H. J., Higgins, C., & van den Bremer, T. S. (2022). The role of the unsteady surface wave-driven Ekman–Stokes flow in the accumulation of floating marine litter. *Journal of Geophysical Research: Oceans*, *127*(6), e2021JC018106. https://doi.org/10.1029/2021JC018106

DiBenedetto, M. H. (2025). The fluid mechanics of ocean microplastics. *Annual Review of Fluid Mechanics*, *58*(1), 355–382. https://doi.org/10.1146/annurev-fluid-120423-012604

Drivdal, M., Broström, G., & Christensen, K. H. (2014). Wave-induced mixing and transport of buoyant particles: Application to the Statfjord A oil spill. *Ocean Science*, *10*(6), 977–991. https://doi.org/10.5194/os-10-977-2014

Gargett, A., Wells, J., Tejada-Martínez, A. E., & Grosch, C. E. (2004). Langmuir supercells: A mechanism for sediment resuspension and transport in shallow seas. *Science*, *306*(5703), 1925–1928. https://doi.org/10.1126/science.1100849

Geyer, W. R., & MacCready, P. (2014). The estuarine circulation. *Annual Review of Fluid Mechanics*, *46*(46), 175–197. https://doi.org/10.1146/annurev-fluid-010313-141302

Gruber, N., Lachkar, Z., Frenzel, H., Marchesiello, P., Münnich, M., McWilliams, J. C., et al. (2011). Eddy-induced reduction of biological production in eastern boundary upwelling systems. *Nature Geoscience*, *4*(11), 787–792. https://doi.org/10.1038/ngeo1273

Hasselmann, K. (1970). Wave-driven inertial oscillations. *Geophysical Fluid Dynamics*, *1*(3–4), 463–502. https://doi.org/10.1080/03091927009365783

Higgins, C., Vanneste, J., & van den Bremer, T. S. (2020). Unsteady Ekman-Stokes dynamics: Implications for surface wave-induced drift of floating marine litter. *Geophysical Research Letters*, *47*(18), e2020GL089189. https://doi.org/10.1029/2020GL089189

Huang, N. E. (1979). On surface drift currents in the ocean. *Journal of Fluid Mechanics*, *91*(1), 191–208. https://doi.org/10.1017/S0022112079000112

Jenkins, A. D. (1986). A theory for steady and variable wind-and wave-induced currents. *Journal of Physical Oceanography*, *16*(8), 1370–1377. https://doi.org/10.1175/1520-0485(1986)016<1370:atfsav>2.0.co;2

Kukulka, T., Plueddemann, A. J., & Sullivan, P. P. (2012). Nonlocal transport due to langmuir circulation in a coastal ocean. *Journal of Geophysical Research*, *117*(C12). https://doi.org/10.1029/2012JC008340

Lenn, Y.-D., & Chereskin, T. K. (2009). Observations of Ekman currents in the southern ocean. *Journal of Physical Oceanography*, *39*(3), 768–779. https://doi.org/10.1175/2008JPO3943.1

Lentz, S. J., Fewings, M., Howd, P., Fredericks, J., & Hathaway, K. (2008). Observations and a model of undertow over the inner continental shelf. *Journal of Physical Oceanography*, *38*(11), 2341–2357. https://doi.org/10.1175/2008JPO3986.1

Lentz, S. J. (1995). Sensitivity of the inner-shelf circulation to the form of the eddy viscosity profile. *Journal of Physical Oceanography*, *25*(1), 19–28. https://doi.org/10.1175/1520-0485(1995)025<0019:sotisc>2.0.co;2

Lewis, D., & Belcher, S. (2004). Time-dependent, coupled, Ekman boundary layer solutions incorporating Stokes drift. *Dynamics of Atmospheres and Oceans*, *37*(4), 313–351. https://doi.org/10.1016/j.dynatmoce.2003.11.001

Lobeto, H., Semedo, A., Lemos, G., Dastgheib, A., Menendez, M., Ranasinghe, R., & Bidlot, J.-R. (2024). Global coastal wave storminess. *Scientific Reports*, *14*(1), 3726. https://doi.org/10.1038/s41598-024-51420-0

Longuet-Higgins, M. S. (1953). Mass transport in water waves. *Philosophical Transactions of the Royal Society of London. Series A, Mathematical and Physical Sciences*, *245*(903), 535–581. https://doi.org/10.1098/rsta.1953.0006

Madsen, O. S. (1978). Mass transport in deep-water waves. *Journal of Physical Oceanography*, *8*(6), 1009–1015. https://doi.org/10.1175/1520-0485(1978)008<1009:mtidww>2.0.co;2

Mellor, G., & Blumberg, A. (2004). Wave breaking and ocean surface layer thermal response. *Journal of Physical Oceanography*, *34*(3), 693–698. https://doi.org/10.1175/2517.1

Mellor, G., & Yamada, T. (1982). Development of a turbulence closure model for geophysical fluid problems. *Reviews of Geophysics*, *20*(4), 851–875. https://doi.org/10.1029/RG020i004p00851

Mol, J., Bayle, P., Duran-Matute, M., & van den Bremer, T. (2025). A laboratory study of wave-induced drift under rotation. *Journal of Fluid Mechanics*, *1017*, A22. https://doi.org/10.1017/jfm.2025.10476

Morales-Caselles, C., Viejo, J., Martí, E., González-Fernández, D., Pragnell-Raasch, H., González-Gordillo, J. I., et al. (2021). An inshore–offshore sorting system revealed from global classification of ocean litter. *Nature Sustainability*, *4*(6), 484–493. https://doi.org/10.1038/s41893-021-00720-8

Moulton, M., Suanda, S. H., Garwood, J. C., Kumar, N., Fewings, M. R., & Pringle, J. M. (2023). Exchange of plankton, pollutants, and particles across the nearshore region. *Annual Review of Marine Science*, *15*(15), 167–202. https://doi.org/10.1146/annurev-marine-032122-115057

Nooteboom, P. D., Bijl, P. K., van Sebille, E., von der Heydt, A. S., & Dijkstra, H. A. (2019). Transport bias by ocean currents in sedimentary microplankton assemblages: Implications for paleoceanographic reconstructions. *Paleoceanography and Paleoclimatology*, *34*(7), 1178–1194. https://doi.org/10.1029/2019PA003606

Phillips, O. M. (1977). *The dynamics of the upper ocean* (2nd ed.). Cambridge University Press. [Book].

Polton, J. A., Lewis, D. M., & Belcher, S. E. (2005). The role of wave-induced Coriolis–Stokes forcing on the wind-driven mixed layer. *Journal of Physical Oceanography*, *35*(4), 444–457. https://doi.org/10.1175/JPO2701.1

Reniers, A., Thornton, E., Stanton, T., & Roelvink, J. (2004). Vertical flow structure during sandy duck: Observations and modeling. *Coastal Engineering*, *51*(3), 237–260. https://doi.org/10.1016/j.coastaleng.2004.02.001

Rühs, S., van den Bremer, T. S., Clementi, E., Denes, M. C., Moulin, A., & van Sebille, E. (2025). Non-negligible impact of Stokes drift and wave-driven Eulerian currents on simulated surface particle dispersal in the Mediterranean sea. *Ocean Science*, *21*(1), 217–240. https://doi.org/10.5194/os-21-217-2025

Sentchev, A., Yaremchuk, M., Bourras, D., Pairaud, I., & Fraunié, P. (2023). Estimation of the eddy viscosity profile in the sea surface boundary layer from underway ADCP observations. *Journal of Atmospheric and Oceanic Technology*, *40*(10), 1291–1305. https://doi.org/10.1175/JTECH-D-22-0083.1

Stokes, G. (1847). On the theory of oscillatory waves. *Transactions of the Cambridge Philosophical Society*, *8*, 441–445.

Ursell, F., & Deacon, G. (1950). On the theoretical form of ocean swell on a rotating earth. *Geophysical Journal International*, *6*(s1), 1–8. https://doi.org/10.1111/j.1365-246X.1950.tb02968.x

van den Bremer, T. S., & Breivik, Ø. (2017). Stokes drift. *Philosophical Transactions of the Royal Society A: Mathematical, Physical and Engineering Sciences*, *376*(2111), 20170104. https://doi.org/10.1098/rsta.2017.0104

van Sebille, E., Aliani, S., Law, K. L., Maximenko, N., Alsina, J. M., Bagaev, A., et al. (2020). The physical oceanography of the transport of floating marine debris. *Environmental Research Letters*, *15*(2), 023003. https://doi.org/10.1088/1748-9326/ab6d7d

Weber, J. E. (1983a). Attenuated wave-induced drift in a viscous rotating ocean. *Journal of Fluid Mechanics*, *137*, 115–129. https://doi.org/10.1017/S0022112083002311

Weber, J. E. (1983b). Steady wind- and wave-induced currents in the open ocean. *Journal of Physical Oceanography*, *13*(3), 524–530. https://doi.org/10.1175/1520-0485(1983)013<0524:swawic>2.0.co;2

Weber, J. E. (2019). Lagrangian studies of wave-induced flows in a viscous ocean. *Deep Sea Research Part II: Topical Studies in Oceanography*, *160*, 68–81. https://doi.org/10.1016/j.dsr2.2018.10.011

Weber, J. E., Drivdal, M., Christensen, K. H., & Broström, G. (2015). Some aspects of the Coriolis-Stokes forcing in the oceanic momentum and energy budgets. *Journal of Geophysical Research: Oceans*, *120*(8), 5589–5596. https://doi.org/10.1002/2015JC010717

Xu, Z., & Bowen, A. J. (1994). Wave- and wind-driven flow in water of finite depth. *Journal of Physical Oceanography*, *24*(9), 1850–1866. https://doi.org/10.1175/1520-0485(1994)024<1850:WAWDFI>2.0.CO;2

Yoshikawa, Y., & Endoh, T. (2015). Estimating the eddy viscosity profile from velocity spirals in the Ekman boundary layer. *Journal of Atmospheric and Oceanic Technology*, *32*(4), 793–804. https://doi.org/10.1175/JTECH-D-14-00090.1